THE ASTROPHYSICAL JOURNAL, 494:419–429, 1998 February 10

A MAGNETOHYDRODYNAMIC DESCRIPTION OF CORONAL HELMET STREAMERS CONTAINING A CAVITY

W. P. GUO AND S. T. WU
Center for Space Plasma and Aeronomic Research and Department of Mechanical and Aerospace Engineering, University of Alabama in Huntsville, Huntsville, AL 35899
Received 1997 May 23; accepted 1997 September 4

ABSTRACT

A three-dimensional axisymmetric time-dependent magnetohydrodynamic model has been used to obtain quasi-static helmet-streamer solutions that contain a cavity flux rope in their closed field region. The dynamical equilibrium of the cavity flux rope inside the closed region of the streamer can be described as the partial balance between the outward acting magnetic force and the pressure and gravity forces inside the flux rope, which, in addition, is held down by the helmet dome above. Our solutions indicate that the helmet streamer containing a cavity flux rope has more magnetic energy than the corresponding open field configuration, which means that the state transition from the former to the latter is permitted energetically. These solutions may serve as pre-event coronae for studying the initiation of coronal mass ejections.

Subject headings: MHD — Sun: corona

1. INTRODUCTION

Coronal helmet streamers are large-scale, quasi-static structures in the solar corona. The observed streamers vary in size and complexity. At solar minimum, the solar corona has the appearance of a large dipole-configuration streamer tilted relative to the solar rotation axis (Hundhausen 1977). Normally, large streamers exhibit a three-part structure, i.e., the high-density dome, the low-density cavity below the dome, and the quiescent prominence inside the cavity (Pneuman & Orrall 1986). Recently, the structure and equilibrium of helmet streamers have been studied closely because of their association with the occurrence of coronal mass ejections (CMEs; Hundhausen 1994; Burkepile & St. Cyr 1993). When coronal streamers erupt, the helmet dome, cavity, and prominence are believed to form, respectively, the leading bright loop, the trailing cavity, and the bright core of the commonly observed looplike CMEs (Illing & Hundhausen 1986).

The observed three-part structure of coronal streamers are believed to reflect the large-scale magnetic field geometry. Observations show that most prominences, especially those associated with helmet streamers, have magnetic fields with inverse polarity (Leroy 1989). The magnetic field generally threads the prominence at a small angle of about 25° with the long axis of the prominence (Tandberg-Hanssen 1995). The strong axial component of the prominence field causes the often observed helical structures in erupting prominences (Vršnak, Ruzdjak, & Rompolt 1991). These observations reflect the fact that there are complex magnetic configurations in the closed region of the streamer. However, in the modeling and simulation of helmet streamers, few authors have addressed the overall magnetic configuration of the streamer cavity prominence as a whole, especially the cavity surrounding the prominence.

Recently, Low (1994) and Low & Hundhausen (1995) proposed that a helmet streamer is indeed a two-flux magnetic system, one flux connecting the bipolar magnetic regions in the photosphere, and the other forming a magnetic flux rope which contains the prominence and runs above the polarity-inversion line. The flux rope manifests itself as the cavity of the helmet streamer and is more fundamental than the prominence it may carry. A schematic description of the streamer-flux-rope configuration is shown in Figure 1. Using this scenario, Low & Hundhausen (1995) were able to model faithfully the observed chromospheric fibril pattern for the first time. This scenario also gained support from the recent *SOHO*/LASCO observations which indicate that some erupted streamers contain disconnected magnetic plasmoids (Simnett et al. 1997; Wu et al. 1997b).

On the other hand, in the study of the initiation of CMEs, it has long been realized that there may not be enough magnetic free energy in the pre-event coronal magnetic structures to fuel such a highly dynamic phenomenon. Aly (1984, 1991) and Sturrock (1991) showed that if a force-free magnetic field is anchored to the surface of the Sun, it cannot have an energy in excess of that in the corresponding fully open configuration. However, a helmet streamer containing a detached magnetic flux rope in its cavity may address this energy problem of CME initiation since the energy in the detached magnetic field is fully available by its expansion to do work on the plasma, while, on the other hand, an anchored bipolar magnetic field absorbs energy as the field lines are stretched out to infinity (Low & Smith 1993).

Recently, we have constructed an MHD model in three-dimensional axisymmetric geometry to investigate the dynamical response of a helmet streamer to the emergence of a helical magnetic flux rope (Wu, Guo, & Dryer 1997a). We find, based on the "magnetic strength" of the flux rope, i.e., the parameters of the initial flux rope before its emergence, three distinct solutions for the emerged flux rope: (1) a quasi-equilibrium solution, (2) a nonequilibrium solution, and (3) an eruptive solution. In the quasi-equilibrium case, we first obtain a self-consistent helmet-streamer solution containing a helical flux rope in its closed field region, as proposed by Low (1994). However, in the above study, the flux rope represents density enhancement rather than a density depletion, which is indicated by observations. In the present study, we present numerical magnetohydrodynamic (MHD) solutions to describe the steady state structures of a coronal helmet streamer containing a

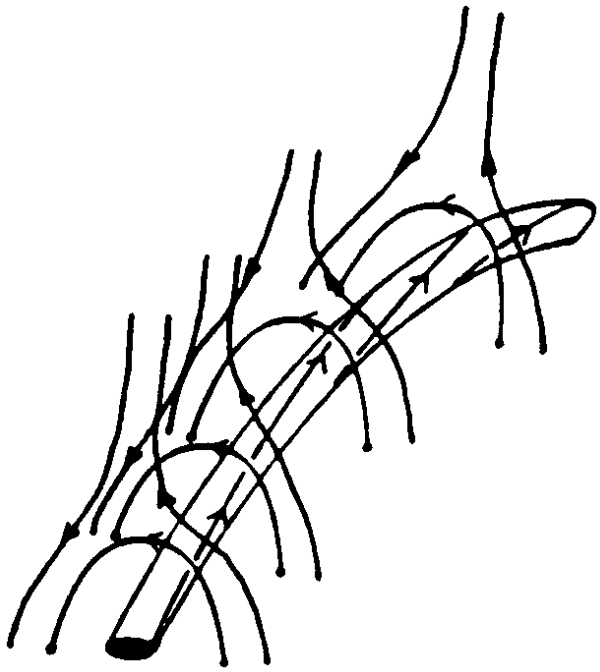

FIG. 1.—Schematic description of the streamer flux rope configuration

cavity flux rope. The mathematical model and method of treatment are given in § 2. The numerical results are discussed in § 3. Finally, concluding remarks are given in § 4.

2. MATHEMATICAL MODEL AND METHOD OF TREATMENT

2.1. *Mathematical Model*

The basic equations in the present study are the single-fluid ideal MHD equations in the system of spherical coordinates (r, θ, φ), where r is the radius, θ the colatitude, and φ the longitude. In axisymmetry [i.e., $(\partial/\partial\varphi) = 0$], the equations can be written as follows:

$$\frac{\partial \rho}{\partial t} = -\frac{1}{r^2}\frac{\partial}{\partial r}(r^2 \rho u_r) - \frac{1}{r \sin\theta}\frac{\partial}{\partial \theta}(\sin\theta \rho u_\theta) ,$$

$$\frac{\partial u_r}{\partial t} = -u_r \frac{\partial u_r}{\partial r} - \frac{u_\theta}{r}\frac{\partial u_r}{\partial \theta} - \frac{1}{\rho}\frac{\partial p}{\partial r} - \frac{1}{r}\left[\frac{\partial}{\partial r}(rB_\theta) - \frac{\partial B_r}{\partial \theta}\right]\frac{B_\theta}{\mu_0 \rho} - \frac{1}{r}\frac{\partial}{\partial r}(rB_\varphi)\frac{B_\varphi}{\mu_0 \rho} - \frac{GM_s}{r^2} + \frac{u_\theta^2 + u_\varphi^2}{r} ,$$

$$\frac{\partial u_\theta}{\partial t} = -u_r \frac{\partial u_\theta}{\partial r} - \frac{u_\theta}{r}\frac{\partial u_\theta}{\partial \theta} - \frac{1}{\rho r}\frac{\partial p}{\partial \theta} + \frac{1}{r}\left[\frac{\partial}{\partial r}(rB_\theta) - \frac{\partial B_r}{\partial \theta}\right]\frac{B_r}{\mu_0 \rho} - \frac{1}{r \sin\theta}\frac{\partial}{\partial \theta}(\sin\theta B_\varphi)\frac{B_\varphi}{\mu_0 \rho} - \frac{u_r u_\theta}{r} + \frac{u_\varphi^2}{r}\cot\theta ,$$

$$\frac{\partial u_\varphi}{\partial t} = -u_r \frac{\partial u_\varphi}{\partial r} - \frac{u_\theta}{r}\frac{\partial u_\varphi}{\partial \theta} + \frac{1}{r \sin\theta}\frac{\partial}{\partial \theta}(\sin\theta B_\varphi)\frac{B_\theta}{\mu_0 \rho} + \frac{1}{r}\frac{\partial}{\partial r}(rB_\varphi)\frac{B_r}{\mu_0 \rho} - \frac{u_r u_\varphi}{r} - \frac{u_\varphi u_\theta}{r}\cot\theta ,$$

$$\frac{\partial B_r}{\partial t} = \frac{1}{r \sin\theta}\frac{\partial}{\partial \theta}[\sin\theta(u_r B_\theta - u_\theta B_r)] ,$$

$$\frac{\partial B_\theta}{\partial t} = -\frac{1}{r}\frac{\partial}{\partial r}[r(u_r B_\theta - u_\theta B_r)] ,$$

$$\frac{\partial B_\varphi}{\partial t} = \frac{1}{r}\frac{\partial}{\partial r}[r(u_\varphi B_r - u_r B_\varphi)] - \frac{1}{r}\frac{\partial}{\partial \theta}(u_\theta B_\varphi - u_\varphi B_\theta) ,$$

$$\frac{\partial T}{\partial t} = -\frac{1}{r^2}\frac{\partial}{\partial r}(r^2 T u_r) - \frac{1}{r \sin\theta}\frac{\partial}{\partial \theta}(T u_\theta \sin\theta) + (2-\gamma)T\left[\frac{1}{r^2}\frac{\partial}{\partial r}(r^2 u_r) + \frac{1}{r \sin\theta}\frac{\partial}{\partial \theta}(u_\theta \sin\theta)\right] . \quad (1)$$

The parameters are u_r, the radial velocity, u_θ, the meridional velocity, and u_φ, the azimuthal velocity; B_r, B_θ, and B_φ, the components of the magnetic field; γ, the polytropic index ($\gamma = 1.05$); μ_0, the magnetic permeability; G, the gravitational constant; M_s, the solar mass; p, the thermal pressure; ρ, the density; and T, the temperature. The equation of state, $p = 2nkT$, is used with n as the number density, and k as the Boltzmann constant.

The computational domain is in the solar meridional plane, extending from 1–6 $R_\odot$, and from pole ($\theta = 0°$) to equator ($\theta = 90°$). We use a nonuniform grid in the r-direction, $\Delta r_i = 0.01745 r_{i-1}$ and a uniform grid in the θ-direction, $\Delta\theta = 1°$, to

obtain a 106 × 92 grid. The MHD equations are discretized by the three-dimensional axisymmetric (i.e., 2.5-dimensional) combined difference scheme which is an extension of the earlier two-dimensional combined difference scheme (Wu, Guo, & Wang 1995). The essence of the combined difference scheme is to use different numerical schemes to treat different MHD equations according to their physical and mathematical characteristics. For instance, the momentum and the magnetic induction equation are solved by using the Lax-Wendroff finite difference scheme. The particular version we used is similar to that given by Rubin & Burstein (1967). An optional semi-implicit operator similar to the one used by Mikić et al. (1988) is used in the momentum equation to study slow evolution cases. In the case of density computation with large gradient near the solar surface, Lax-Wendroff scheme is not very stable. Thus, we used the second type upwind scheme by considering the advective nature of the continuity equation. Since we used a staggered grid to achieve high accuracy and to avoid sawtooth oscillations, subsequently, the upwind scheme achieved second order accuracy. For the energy equation, we also used the upwind scheme to discretize its advective terms. All these procedures are aiming for better numerical accuracy by taking into account the physical and mathematical characteristics of the governing equations.

The computational domain has four boundaries. Symmetric boundary conditions are used at the pole and the equator. At the inner boundary, the flow is subsonic and sub-Alfvénic. The method of projected normal characteristics (Wu & Wang 1987) are used to prescribe the inner boundary conditions. At the outer boundary, linear extrapolation is used since the flow is supersonic and super-Alfvénic.

2.2. *Method of Treatment*

Three steps are necessary to construct the helmet-streamer solutions containing a cavity flux rope.

The first step is to obtain normal helmet-streamer solutions. We have chosen two solutions for the present study. They are dipole-configuration quasi-equilibrium helmet streamers obtained using the time-relaxation method (Steinolfson, Suess, & Wu 1982). The physical parameters at the bottom boundary are the following. Case 1: $n_0 = 3.2 \times 10^8$ cm^{-3}, $T_0 = 1.8 \times 10^6$ K, and the magnetic field is a dipole with $B_0 = 2.0$ G at the equator, which corresponds to $\beta = 1.0$ at the equator and $\beta = 0.25$ at the pole. Case 2: $n_0 = 3.2 \times 10^8$ cm^{-3}, $T_0 = 1.8 \times 10^6$ K, and $B_0 = 2.83$ G, which corresponds to $\beta = 0.5$ at the equator and $\beta = 0.125$ at the pole. The magnetic field lines and velocities of the two initial streamers are shown in Figure 2. Figure 3 shows the corresponding integrated line-of-sight brightness (pB) which is obtained by integrating the Thomson scattering of photospheric light using computed density along the line of sight.

The second step is to obtain helmet-streamer solutions containing a flux rope based on the solutions obtained in step 1. The mathematical procedure to obtain this solution is first to construct a helical magnetic torus and then to move it into the closed field region of the initial streamer obtained in the first step. To carry out this process, we simply change the physical variables at the inner boundary according to the magnetic torus solution. Physically, this could be thought of as a simulation of the emergence of flux ropes from below the photosphere into the corona since the recent observations suggest that magnetic flux may indeed emerge as a nearly closed system (Lites et al. 1995). It should be noted that the magnetic torus solution cannot be directly superimposed onto the streamer solution obtained in step 1 because it will promptly disrupt the solution due to the mismatch in density and magnetic field. This will cause numerical instability which will make it impossible for the system to relax to a new equilibrium state.

An equilibrium solution given by Shafranov (1960) is used to construct the magnetic torus before its emergence. The details of this solution are listed in the Appendix. The parameters of the magnetic torus used for the two cases are listed in Table 1. In Table 1, a is normalized to $R_\odot$, p_0 is normalized to $p_\odot$, the pressure at the inner boundary (i.e., 1 $R_\odot$).

The process of torus emergence consists of two substeps. First, place the torus below the initial streamer at $r = R_\odot - a$. Then, move it outward very slowly with $V = 9.7$ km s^{-1} (i.e., $0.04 v_A$; v_A is the local Alfvén speed) into the closed region of the initial streamer. It takes 4 hr for the torus to move completely into the computational domain for both cases. Computationally, this process is simulated by the changes of the physical parameters based on the torus solution at the inner boundary. Wu et al. (1995) have discussed the details of the actual implementation. We have chosen the appropriate parameters of the torus so that after the magnetic torus has moved into the closed region of the streamer, the streamer-flux-rope configuration reaches a quasi-equilibrium state. Figure 4 shows the magnetic field and velocity distribution of the streamer-flux-rope configuration 12 hr after the flux rope emergence for the two cases in which the quasi-equilibrium state is established. (Figs. 8*a* and 9*a* below show the polarization brightness of the two streamer-flux-rope configurations.)

The final step is to obtain helmet-streamer solutions containing a cavity flux rope. The procedure to reach this solution is to take the solutions obtained in the previous step (as shown in Figs. 8*a* and 9*a*) by removing part of the mass contained in the flux rope and simultaneously increase the azimuthal magnetic field of the flux rope in order to keep its pressure balance with the streamer. Physically, this process could be thought of as the mass draining occurring in the dynamic evolution of a filament.

TABLE 1

PARAMETERS OF MAGNETIC TORUS FOR TWO CASES

Case	a	p_0	β_1	β_2
1.....	0.1	1.0	0.55	0.22
2.....	0.1	1.0	0.25	0.1

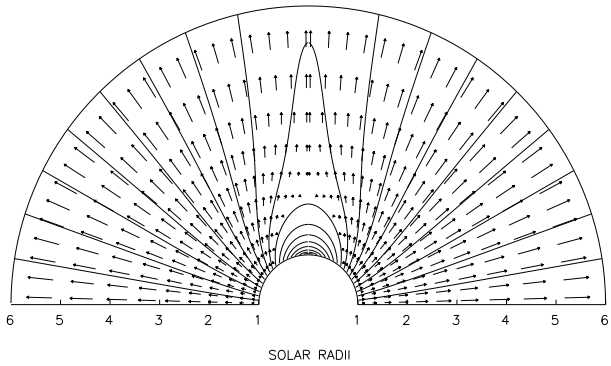

FIG. 2*a*

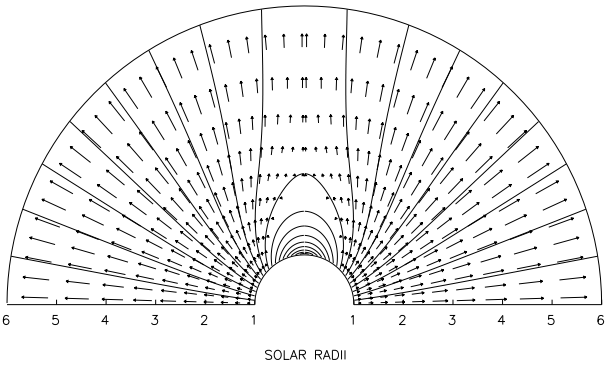

FIG. 2*b*

FIG. 2.—Magnetic field configuration (*solid lines*) and velocities (*arrows*) of the initial streamer for case 1(*a*) and case 2(*b*) ($t = 0$ hr)

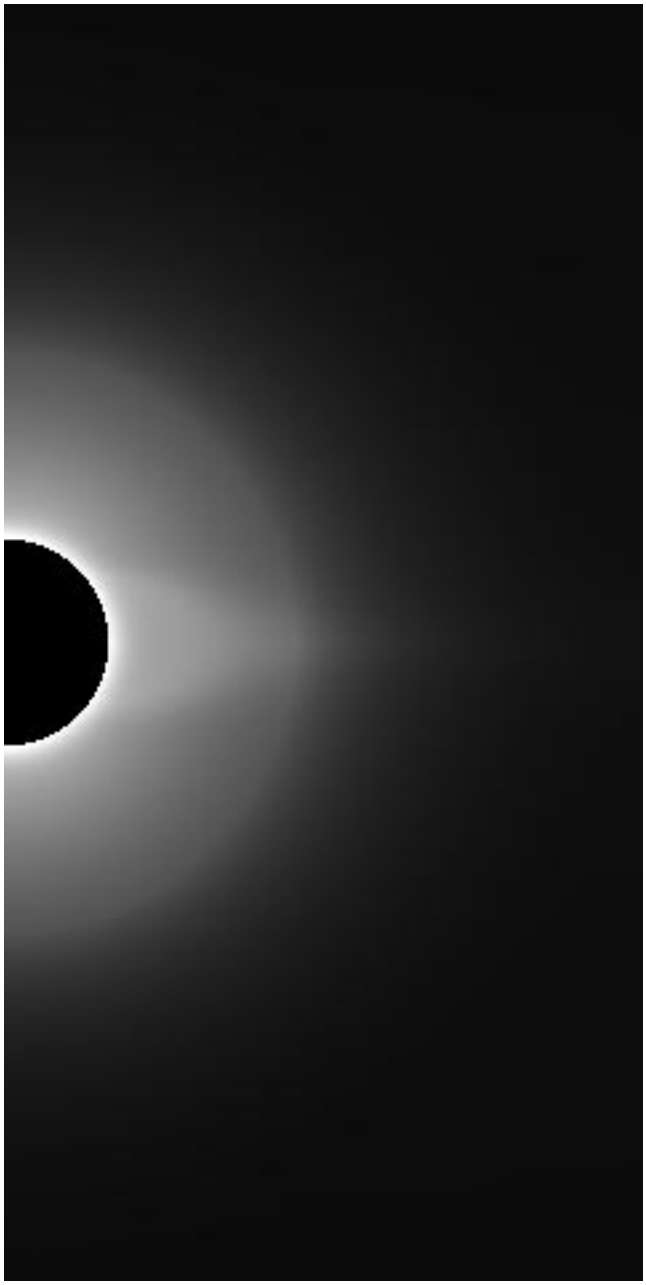

FIG. 3*a*

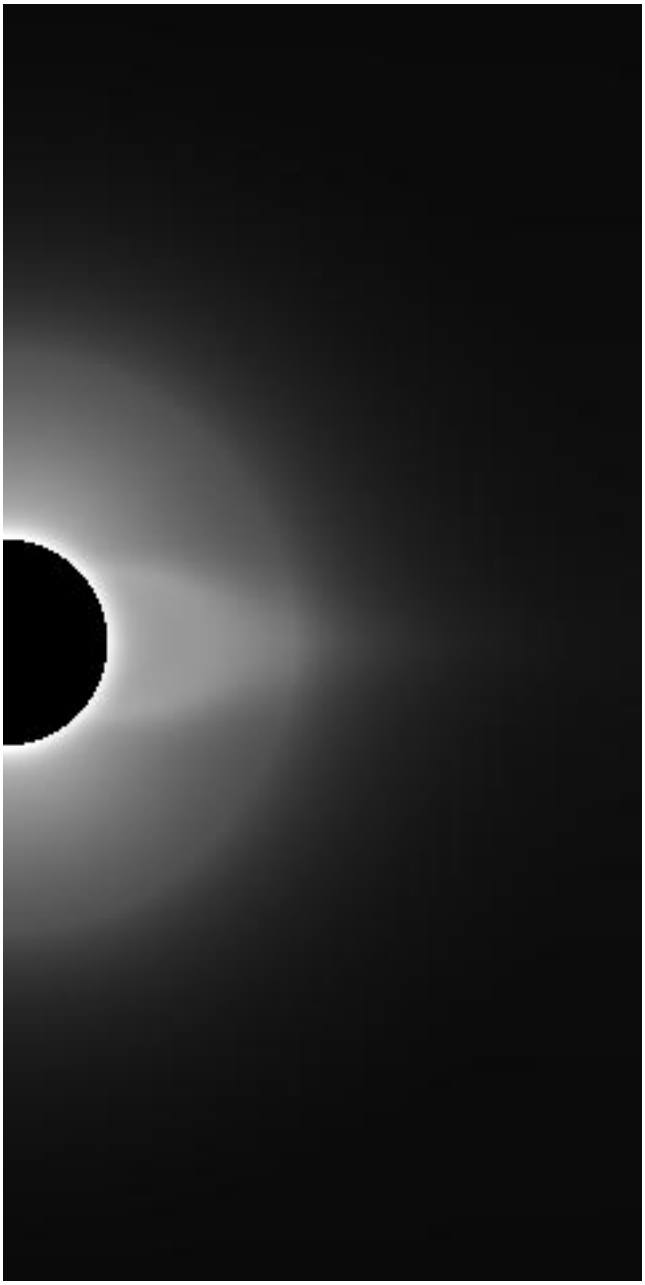

FIG. 3*b*

FIG. 3.—Integrated line-of-sight brightness (i.e., pB) of the two initial streamers ($t = 0$ hr). Position of the Sun is indicated by the dark half-circle at the center. The radius of the half circle is 1 $R_\odot$. Case 1 is shown in (*a*), and case 2 in (*b*).

The changes in the density ρ and the azimuthal magnetic field B_φ in the flux rope are given by

$$\rho^{n+1} = \rho^n \left[1 - \delta \left(1 - \frac{r^*}{0.85 r_f} \right) \right], \tag{2}$$

$$B_\varphi^{n+1} = B_\varphi^n \left[1 + \delta \left(1 - \frac{r^*}{0.85 r_f} \right) \right], \tag{3}$$

where r_f is the radius of the flux rope, the superscript "n" indicates the time step, δ is a constant related to the magnitude of change at each time step, r^* is the distance between the center of the flux rope and a point within the flux rope, where its ρ and B_φ are changed. In the present study, we choose $r^* < 0.85 r_f$ and $\delta = 0.0015$.

In our computation, once the quasi-equilibrium streamer-flux-rope solution described in the previous step was obtained, we use numerical procedure to drain the mass and increase B_φ using equations (2) and (3). After 5 hr, we stop this process and let ρ and B_φ be determined by the ideal MHD equations. Since the rate of change (i.e., δ) is very small, the streamer flux rope retains its overall configuration during the mass-draining process. It should be noted that since our model is a three-dimensional axisymmetric model, a change in B_φ does not affect the solenoidal condition ($\nabla \cdot \boldsymbol{B} = 0$). However, in order to assure the high accuracy of the solenoidal condition numerically, the divergence-cleaning procedure proposed by Ramshaw (1983) is again employed in the present calculation.

After the mass-draining process, the original quasi-equilibrium solution of streamer-flux rope with density enhancement relaxed to a quasi-equilibrium solution of streamer-flux rope with a cavity. The details of the streamer-cavity solution will be discussed in the following section.

3. NUMERICAL RESULTS AND DISCUSSION

In the previous section, we discussed the procedures to obtain quasi-equilibrium helmet streamers containing a cavity flux rope in their closed field region. In this section, we shall discuss the physical details of the obtained solutions.

3.1. *Density Feature and Field Configuration*

Figures 5 and 6 show the magnetic field and velocity configurations in the meridional plane after mass draining for the two cases. Comparing with the corresponding configuration before mass draining, we see that after mass draining, the whole configuration is still in equilibrium, although the flux rope expands a little. The flux rope is still confined by the closed streamer field from above. Figures 5 and 6 also show the time evolution of the streamer-cavity solutions. Comparing Figures 5*a* and 6*a* with Figures 5*b* and 6*b*, we notice that the two streamer-cavity solutions reach quasi-equilibrium states. In Figure 7, we plot the three-dimensional magnetic field of the streamer-flux-rope configuration and the integrated line of sight brightness (pB) for case 2. This figure clearly demonstrates the three-dimensional nature of the flux rope.

The integrated line-of-sight brightness before and after the mass draining for the two cases are shown in Figures 8 and 9. It is clear that after mass draining, the density enhancement in the closed region of the streamer changed into a cavity as indicated by Figures 8*b* and 9*b*. Part of the thermal pressure in the flux rope is then replaced by magnetic pressure. We computed the plasma β at the center of the flux rope before and after mass draining. For case 1, β changed from 0.33 to 0.12; for case 2, β changed from 0.29 to 0.16. In our simulation, we also tested the cases in which only mass draining takes place in the flux rope without increasing the magnetic field strength. In these cases, the flux rope collapses. Our test results suggest that the cavity must contain enough magnetic strength for its existence.

3.2. *Force Balance*

To study the force balance of the flux rope within the helmet streamer, we plot in Figure 10 the radial distribution of the combined forces of pressure and gravity, and the magnetic force for the two cases. From this figure, we notice that at the upper half of the flux rope, i.e., 1.38–1.74 $R_\odot$ for case 1 and 1.41–1.68 $R_\odot$ for case 2, the upward magnetic force balances the downward combined forces. At the lower half, i.e., 1–1.38 $R_\odot$ for case 1 and 1–1.41 $R_\odot$ for case 2, the upward combined forces

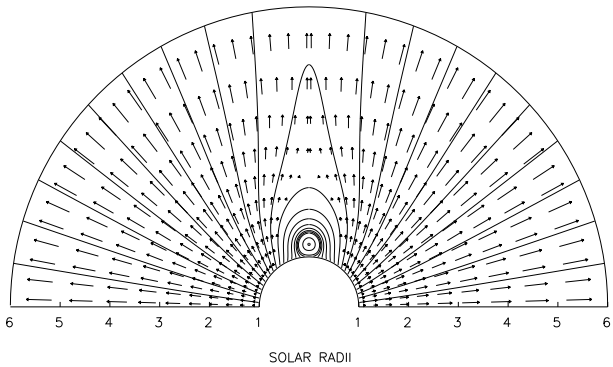

FIG. 4*a*

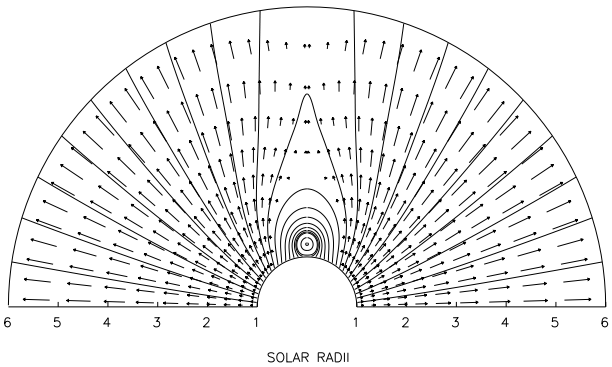

FIG. 4*b*

FIG. 4.—Magnetic field and velocity configurations after the emergence of the magnetic flux rope for the two cases (t = 12 hr). Case 1 is shown in (*a*), and case 2 is shown in (*b*).

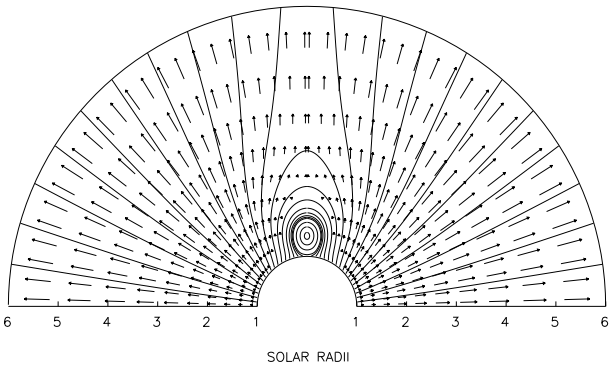

FIG. 5*a*

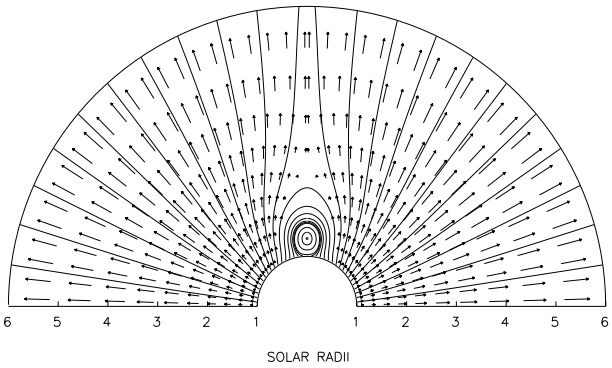

FIG. 5*b*

FIG. 5.—Time evolution of the magnetic field and velocity configurations of the helmet streamer containing a cavity flux rope for case 1 at $t = 18$ hr (*a*) and $t = 32$ hr (*b*).

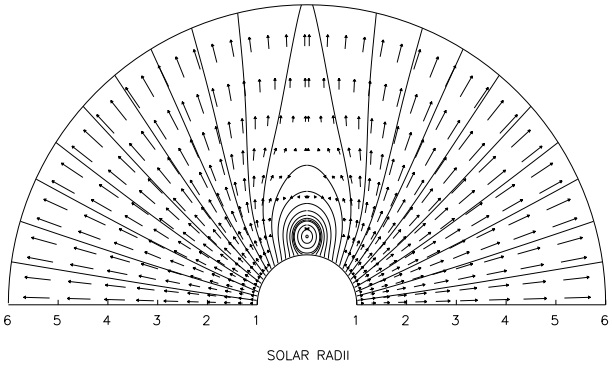

FIG. 6*a*

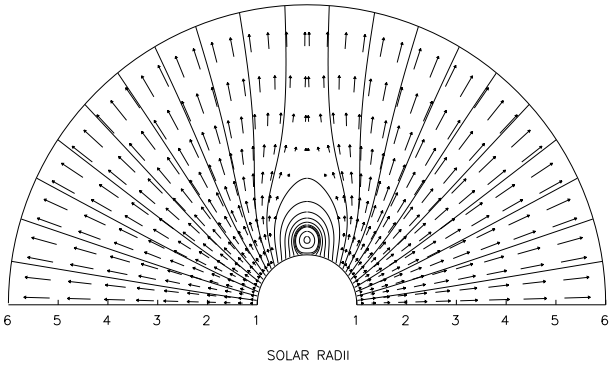

FIG. 6*b*

FIG. 6.—Time evolution of the magnetic field configuration and velocity of the helmet streamer containing a cavity flux rope for case 2 at $t = 18$ hr (*a*) and $t = 32$ hr (*b*).

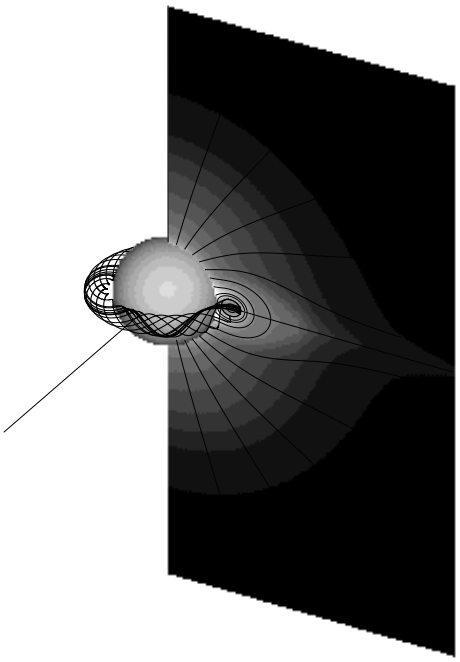

FIG. 7.—Three-dimensional magnetic field configuration of the streamer flux rope structure and the integrated line-of-sight brightness (pB) for case 2 at $t = 22$ hr. The ball at the center represents the Sun. The magnetic field lines of the streamer and the line of sight brightness are projected onto a plane. In the present model, the flux rope in the closed field region of the streamer is actually a magnetic torus circling around the Sun.

balance the downward magnetic force. Above the flux rope in the helmet dome, the upward combined forces balance the downward magnetic force.

Our results indicate that magnetically, the flux rope is trying to expand. However, this tendency is partially balanced by the pressure and gravity inside the flux rope. Above the flux rope, the anchored field in the helmet dome also plays an important role in confining the flux rope. This scenario agrees well with the qualitative description given by Low & Hundhausen (1995) from a theoretical point of view. Low & Hundhausen assumed that the cavity is a magnetic flux rope and showed that an inverse-polarity type prominence cannot exist without its associated cavity, although a cavity without a prominence is a realizable equilibrium state. In the present paper, we actually obtain two self-consistent MHD solutions of a helmet streamer containing a cavity flux rope with background solar wind. However, in the present stage of global-scale MHD simulation, we cannot resolve the actual scale of a prominence that may exist in the flux rope. If a prominence is present, we may build up more magnetic energy in the flux rope since the high-density prominence acts as an anchor of the light flux rope.

3.3. *Magnetic Energy Content*

To discuss the magnetic energy content of the streamer-flux-rope configurations, we numerically integrated their magnetic

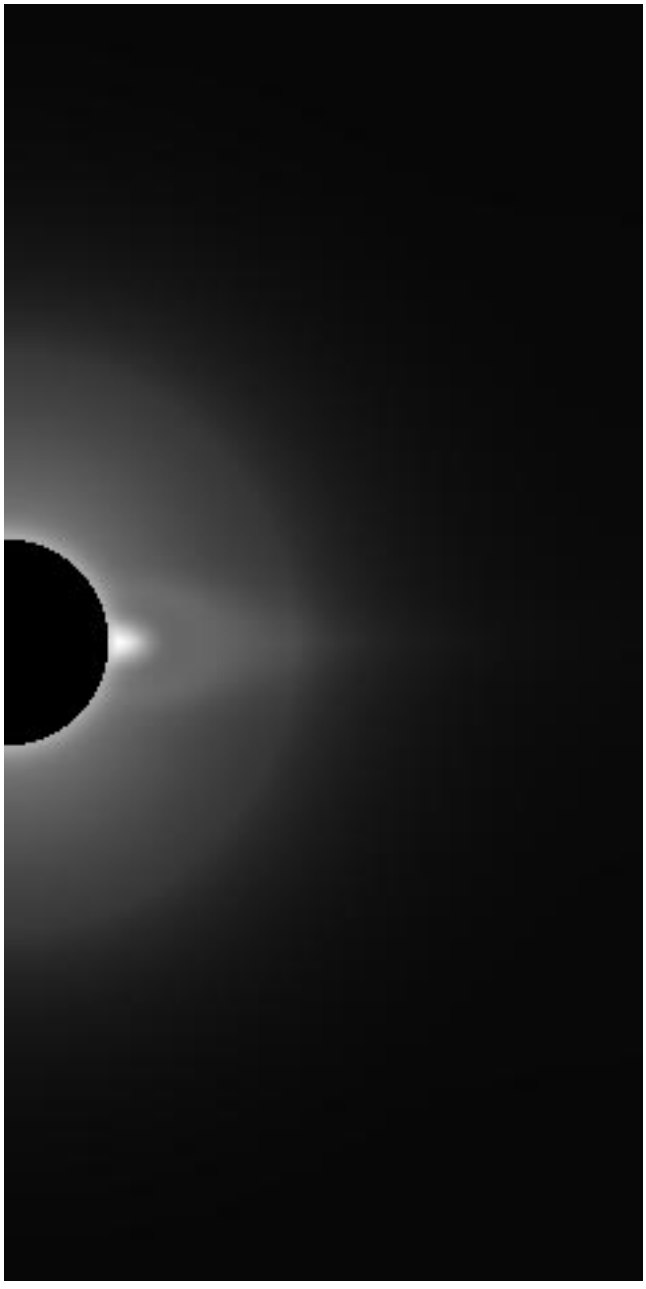

FIG. 8*a*

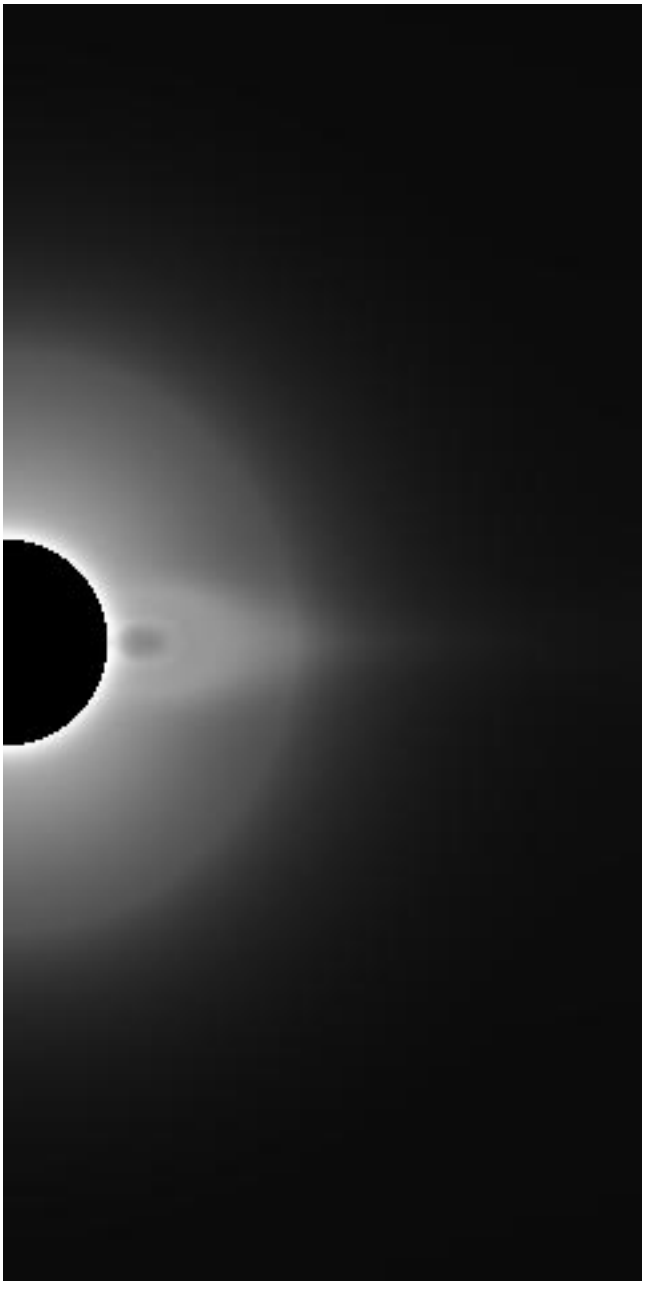

FIG. 8*b*

FIG. 8.—Integrated line-of-sight brightness (pB) for case 1, (*a*) the helmet streamer containing a flux rope with density enhancement at $t = 12$ hr, (*b*) the helmet streamer containing a flux rope with cavity at $t = 22$ hr. Note the dark void below the helmet dome.

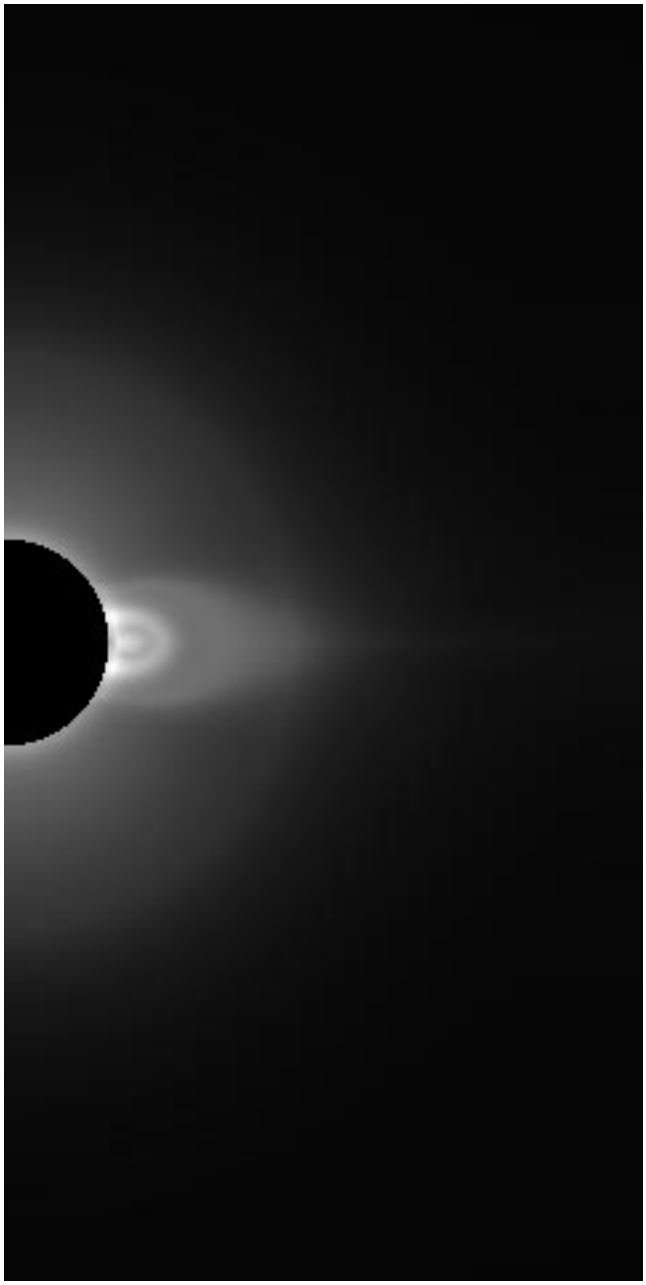

FIG. 9*a*

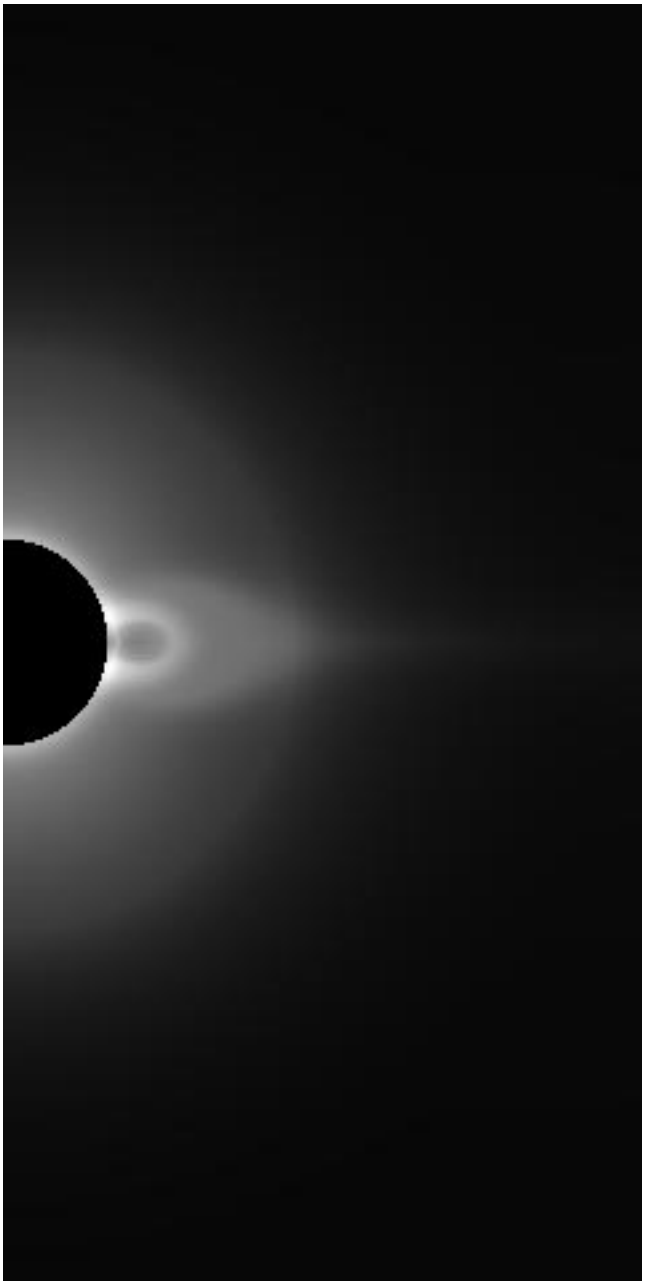

FIG. 9*b*

FIG. 9.—Integrated line-of-sight brightness (pB) for case 2, (*a*) the helmet streamer containing a flux rope with density enhancement at $t = 12$ hr, (*b*) the helmet streamer containing a flux rope with cavity at $t = 22$ hr. Compared to Fig. 8, the dark void in this case is more prominent.

energy content in our computational domain (1–6 $R_\odot$) using the following formula:

$$E_B = \int_0^{2\pi} \int_0^{\pi} \int_1^{6} \frac{B^2}{2\mu_0} r^2 \sin\theta \, dr \, d\theta \, d\varphi \, . \tag{4}$$

Table 2 shows the ratio of the magnetic energy in different configurations to its corresponding potential state for the two cases. It is obvious that the streamer-flux-rope configurations have much more magnetic energy than the corresponding initial

TABLE 2

MAGNETIC ENERGY CONTENT OF DIFFERENT STATES [E_B/E_B(potential)]

Case	Initial Streamer	Streamer Flux Rope (Density Enhancement)	Streamer Flux Rope (Cavity)	Open State
1.....	1.076	1.434	1.592	1.490
2.....	1.035	1.467	1.549	1.464

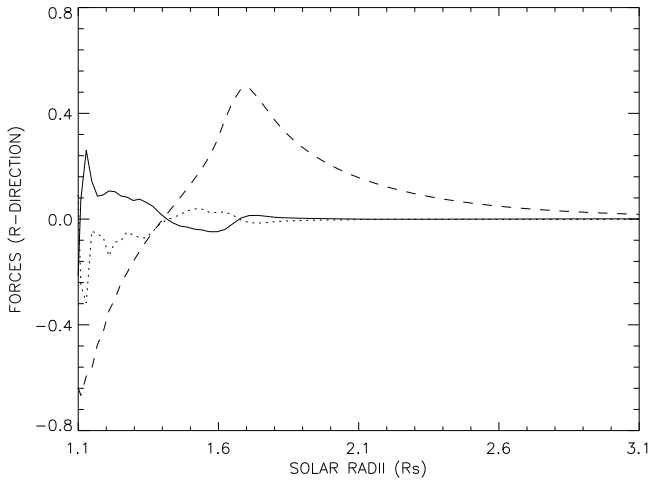

FIG. 10*a*

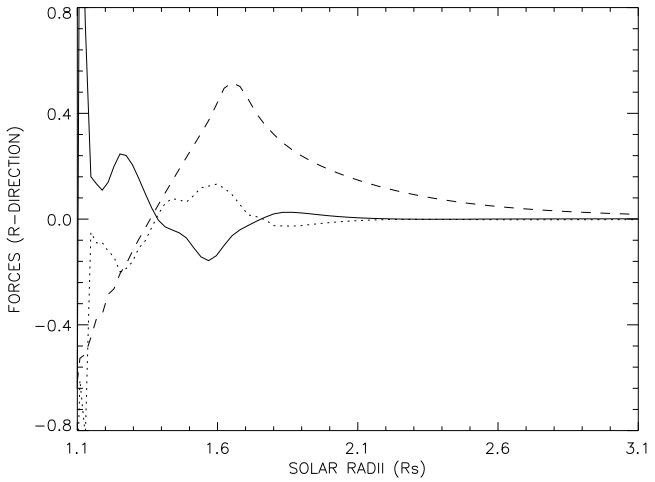

FIG. 10*b*

FIG. 10.—Radial distribution of the combined forces of pressure gradient and gravity (*solid line*) and magnetic force (*dotted line*) for the two cases at $t = 18$ hr and 6°.5 from the equator. Case 1 is shown in (*a*), and case 2 is shown in (*b*). Dashed line represents the radial distribution of B_θ, $B_\theta = 0$ indicates the center of the flux rope.

streamers. The helmet streamer containing a cavity flux rope has more magnetic energy than the corresponding streamer containing a flux rope with density enhancement. This additional energy increase is due to the increase of the azimuthal component of the magnetic field in the flux rope.

In Table 2, we also show the magnetic energy of the corresponding open field configuration. The open configuration is deduced numerically from the initial streamer by keeping the magnetic flux distribution at the solar surface constant and adding a radial velocity at the solar surface to blow open the closed field lines of the streamer. After about 30 hr, the solution reaches quasi-equilibrium and almost all of the field lines become radial. We call this state the corresponding open state. Figure 11 shows the magnetic field and velocity configurations of the open state for case 1, which corresponds to Figure 2*a*. This open state is a self-consistent solution derived from the full set of ideal MHD equations. Using the expedient suggested by Barnes & Sturrock (1972), Mikić & Linker (1994) computed the magnetic energy of the fully open field configuration associated with a dipole potential field. They found that $E_{\rm open} = 1.662E_{\rm potential}$ which is substantially higher than the open field energy we obtain. This discrepancy, we believe, is due to the different integration regions used. The integration region they used is from 1 $R_\odot$ to infinity while our integration region is confined by our computational domain, namely, from 1–6 $R_\odot$. To verify that our open field configuration has energy comparable to their solution, we extended our computation domain to 32 $R_\odot$ and recomputed the open state corresponding to case 1. The integrated open state energy is $1.714E_{\rm potential}$.

It should be noted that for both cases, the magnetic energy of the streamer-cavity-flux-rope configuration exceeds the corresponding open state energy. The state transition from the former to the latter therefore is permitted energetically.

4. CONCLUSION

We have used a three-dimensional axisymmetric time-dependent MHD model to obtain quasi-static helmet streamers containing a cavity flux rope in their closed field region. Two solutions were obtained based on different parameters of the initial streamer. The dynamical equilibrium of the cavity flux rope inside the closed region of the streamer can be described as the partial balance between the outward acting magnetic force and the pressure and gravity force inside the flux rope, which,

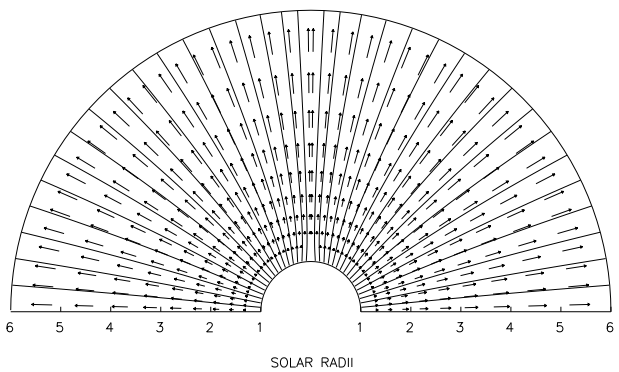

FIG. 11.—Magnetic field lines and velocity distribution of the open state corresponding to Fig. 2*a*. This open state is a self-consistent MHD solution.

in addition, is held down by the heavy helmet dome above. Our results also indicate that the helmet streamer containing a cavity flux rope may have more magnetic energy than the corresponding open field configuration, which makes the state transition of the streamer possible without an external energy source. In the present model, the flux rope is a wholly detached structure circling the Sun as shown in Figure 7. For a fully three-dimensional description, the flux rope must have both ends connected to the photosphere.

The solutions obtained in this paper can be used as initial states to study the initiation of coronal mass ejections (Wu & Guo 1997; Wu et al. 1997). More parametric studies should be done concerning the stability and energy content of the helmet streamer containing a cavity flux rope. A recent study using self-similar MHD to construct a three-dimensional flux rope solution without explicit streamer structure and background solar wind has been given by Gibson & Low (1997). Our future efforts will use the present methodology to extend our study to three dimensions to complement the self-similar MHD study.

We are indebted to E. Tandberg-Hanssen for reading the manuscript and making invaluable suggestions. The work done by W. P. G. and S. T. W. was supported by a National Science Foundation Grant ATM 96-33629, NASA grant NAG 5-6174 and by NRL through USRA N00014-C-95-2058.

APPENDIX

AXISYMMETRIC MAGNETIC TORUS SOLUTION

An axisymmetric magnetic toroid solution given by Shafranov (1960) is used in the present simulation. This solution describes an equilibrium magnetic torus which satisfies the Grad-Shafranov equation in the approximation of small curvature (see Shafranov 1960 for details). The expressions of this solution for plasma pressure (p) and magnetic field ($\boldsymbol{B}$) in cylindrical coordinates are:

$$p = \frac{1}{4\pi^2 a^2} J_\varphi J_p \left[1 - \frac{4R^2}{a^2}\frac{(r-R)^2 + z^2}{\delta}\right] + \frac{1}{2\pi^2 a^2} J_p \left(J_p + \frac{5}{4} J_\varphi\right)\left[1 - \frac{4R^2}{a^2}\frac{(r-R)^2 + z^2}{\delta}\right]\frac{r^2 - R^2 + z^2}{\delta} + p_0 , \quad \text{(A1)}$$

$$B_r = \left(\frac{\beta_0}{2}\right)^{1/2} \frac{8R^4 z}{\pi a^2 \delta^2} J_\varphi - \left(\frac{\beta_0}{2}\right)^{1/2} \frac{R}{2\pi r}\left(J_p + \frac{5}{4} J_\varphi\right)\left\{\frac{r^2 - R^2 + z^2}{\delta}\left(-\frac{32rzR^3}{a^2\delta^2}\right) + \frac{4Rz(R+r)}{\delta^2}\left[1 - \frac{4R^2}{a^2}\frac{(r-R)^2 + z^2}{\delta}\right]\right\}, \quad \text{(A2)}$$

$$B_z = -\left(\frac{\beta_0}{2}\right)^{1/2} \frac{4R^4(r^2 - R^2 - z^2)}{\pi a^2 r \delta^2} J_\varphi + \left(\frac{\beta_0}{2}\right)^{1/2} \frac{R}{2\pi r}\left(J_p + \frac{5}{4} J_\varphi\right) \times \left\{\frac{(r^2 - R^2)^2 - z^4}{\delta}\left(-\frac{16R^3}{a^2\delta^2}\right) + \frac{2R(R^2 + r^2 + 2rR - z^2)}{\delta^2}\left[1 - \frac{4R^2}{a^2}\frac{(r-R)^2 + z^2}{\delta}\right]\right\}, \quad \text{(A3)}$$

$$B_\varphi = \frac{R}{r}\sqrt{\frac{J_\varphi - J_p}{J_p}\beta_0(p - p_0)} , \quad \text{(A4)}$$

with $\beta_0 = (2\mu_0 p_s/B_s^2)^{1/2}$, $\delta = (r + R)^2 + z^2$; J_φ and J_p are constants, representing total and partial current. The radius, pressure, magnetic field, and currents are normalized, as follows:

$$R' = r/R_\odot , \quad p' = p/p_\odot , \quad B'_r = B_r/B_\odot , \quad B'_z = B_z/B_\odot , \quad B'_\varphi = B_z/B_\odot ,$$
$$J'_\varphi = J_\varphi \Big/ \left(\frac{R_\odot^2 p_0}{\mu_0}\right)^{1/2} , \quad J'_p = J_p \Big/ \left(\frac{R_\odot^2 p_0}{\mu_0}\right)^{1/2} , \quad \text{(A5)}$$

with $R_\odot$, $p_\odot$, and $B_\odot$ being solar radius, plasma pressure, and magnetic field strength on the solar surface, respectively. For convenience, the prime is dropped in equations (A1)–(A4) which are the final expressions for an axisymmetric magnetic toroid in cylindrical coordinates. In order to introduce these expressions into the present simulation, we transform them into spherical coordinates (r, θ, φ). The parameters defining the flux rope are a, the flux rope radius; R, the large radius (the center of the torus refers to the center of the Sun); p_0, thermal pressure at the surface of the torus; β_1, plasma β at the central axis of the torus; and β_2, plasma β at the surface of the torus. For convenience, constants J_φ and J_p are replaced by β_1 and β_2 which have clearer physical meaning. We set $R = R_\odot$ in the torus solution, and only four parameters are left to determine the solution.

REFERENCES

Aly, J. J. 1984, ApJ, 283, 349
———. 1991, ApJ, 375, L61
Barnes, C. W., & Sturrock, P. A. 1972, ApJ, 174, 659
Burkepile, J. T., & St. Cyr, C. D. 1993, Natl. Cent. Atmos. Research Tech. Note (nr369 + STR)
Gibson, S. E., & Low, B. C. 1998, ApJ, 493, 460
Hundhausen, A. J. 1977, in Coronal Holes and High Speed Wind Streams, ed. J. Zirker (Boulder: Colorado Assoc. Univ. Press), 225
Illing, R. M. E., & Hundhausen, A. J. 1986, J. Geophys. Res., 91, 10951
Leroy, J. L., 1989, in Dynamics and Structure of Quiescent Solar Prominences, ed. E. R. Priest (Dordrecht: Kluwer), 77
Lites, B. W., Low, B. C., Martinez Pillet, V., Seagraves, P., Skumanich, A., Frank, Z. A., Shine, R. A., & Tsuneta, S. 1995, ApJ, 446, 877
Low, B. C. 1994, Phys. Plasmas, 1, 1684
Low, B. C., & Hundhausen, J. R. 1995, ApJ, 443, 818
Low, B. C., & Smith, D. F. 1993, ApJ, 410, 412

Mikić, E., Barnes, D. C., & Schnack, D. D. 1988, ApJ, 328, 830
Mikić, Z., & Linker, J. A. 1994, ApJ, 430, 898
Pneuman, G. W., & Orrall, F. Q., 1986, in Physics of the Sun, Vol. 2, ed. P. A. Sturrock, T. E. Holzer, D. M. Mihalas, & R. K. Ulrich (Dordrecht: Reidel), 100
Ramshaw, J. D. 1983, J. Comp. Phys., 52, 592
Rubin, E. L., & Burstein, S. Z. 1967, J. Comput. Phys., 2, 178
Shafranov, V. D. 1960, Soviet Phys. JETP, 37, 775
Simnett, G. M., et al. 1997, Sol. Phys., in press
Steinolfson, R. S., Suess, S. T., & Wu, S. T. 1982, ApJ, 255, 730
Sturrock, P. A. 1991, ApJ, 380, 655
Tandberg-Hanssen, E. 1995, The Nature of Solar Prominences (Dordrecht: Kluwer)
Vršnak, B., Ruzdjak, V., & Rompolt, B. 1991, Sol. Phys., 136, 151
Wu, S. T., & Guo, W. P. 1997, in AGU Geophys. Monogr. Ser. 99, Coronal Mass Ejections: Causes and Consequences, ed. N. Crookeer, J. Joselyn, & J. Feynman (Washington, DC: AGU), 83
Wu, S. T., et al. 1997b, Sol. Phys., in press
Wu, S. T., Guo, W. P., & Dryer, M. 1997a, Sol. Phys., 170, 265
Wu, S. T., Guo, W. P., & Wang, J. F. 1995, Sol. Phys., 157, 325
Wu, S. T., & Wang, J. F. 1987, Comput. Methods Appl. Mech. Eng., 64, 267